Earth and Planetary Science Letters 550 (2020) 116543

Contents lists available at ScienceDirect

Earth and Planetary Science Letters

www.elsevier.com/locate/epsl

Interpretation of topography and bed properties beneath Thwaites Glacier, West Antarctica using seismic reflection methods

Elisabeth R. Clyne [a,*], Sridhar Anandakrishnan [a], Atsuhiro Muto [b], Richard B. Alley [a], Donald E. Voigt [a]

[a] Dept. of Geosciences and the Earth and Environmental Systems Institute, The Pennsylvania State University, University Park, PA 16802, USA
[b] Dept. of Earth and Environmental Sciences, Temple University, Philadelphia, PA, USA

ARTICLE INFO

Article history:
Received 30 March 2020
Received in revised form 8 July 2020
Accepted 21 August 2020
Available online 4 September 2020
Editor: M. Ishii

Dataset link:
https://doi.org/10.26207/6tj1-a971

Keywords:
Thwaites Glacier
West Antarctica
reflection seismic
bed character
till properties
acoustic impedance

ABSTRACT

Thwaites Glacier (TG), West Antarctica, is losing mass in response to oceanic forcing. Future evolution could lead to deglaciation of the marine basins of the West Antarctic Ice Sheet, depending on ongoing and future climate forcings, but also on basal topography/bathymetry, basal properties, and physical processes operating within the grounding zone. Hence, it is important to know the distribution of bed types of TG's interior and grounding zone, and to incorporate them accurately in models in order to improve estimates of retreat rates and stability. Here we estimate properties of the bed by determining its acoustic impedance from amplitude analysis of reflection seismic data. We report on the results from two lines – a longitudinal (L-Line) and a transverse (N-Line) – on a central flowline of TG ~100 km inland from the grounding zone. The data show considerable spatial variability in bed forms and properties, similar to results from a comparable survey farther inland. Notably, we find the same pattern here of hard (presumed bedrock) material on the stoss side of bumps and soft (presumed till) on the lee side. Physical understanding indicates the basal flow law describing motion over different regions of TG's bed likely varies from nearly-viscous over the bedrock regions to nearly-plastic over till regions, providing guidance for modeling.

1. Introduction

Thwaites Glacier (TG), located in the West Antarctic Ice Sheet (WAIS), drains a basin with ~0.65 m sea-level-equivalent ice (Rignot et al., 2019), and could potentially lead to the deglaciation of the majority of the marine basins of WAIS and sea-level rise of more than 3 m (reviewed by Alley et al., 2015; Scambos et al., 2017). TG terminates in the Amundsen Sea (Fig. 1), where ocean temperatures are influenced by changes in circulation of the relatively warm Circumpolar Deep Water onto the continental shelf and extending below the TG ice shelf (Jenkins et al., 2016; Holland et al., 2019). Recent increase in this circulation has led to greater basal melting of ice shelves in the Amundsen Sea embayment including the TG shelf (Rignot and Jacobs, 2002; Shepherd et al., 2004; Holland et al., 2019). The resulting loss of buttressing for the grounded ice has led to faster ice flow and accelerating inland migration of the grounding line (e.g., Christianson et al., 2016; Scambos et al., 2017). If the TG ice shelf melts or calves off to a significant degree, the ice sheet may be exposed to the ocean at the grounding line and could be susceptible to rapid calving there (Bassis and Walker, 2012; Pollard et al., 2015; Parizek et al., 2019).

The sensitivity of ice-sheet response to climate forcing depends importantly on the topography and rheology of the bed beneath the grounded ice. While the grounding zone of TG currently rests on a stabilizing sill (topographic high), modeling indicates that ice-shelf loss may have already committed TG to destabilization if the bed is treated as nearly viscous (Joughin et al., 2014). With a linear-viscous bed (e.g., sliding over a hard bed; Weertman, 1957), thinning is localized near the coast, allowing the ice to float off the stabilizing sill and the grounding zone to rapidly retreat inland (Parizek et al., 2013). If the bed is treated as more-nearly plastic, then thinning can rapidly propagate upstream and tap into ice from a larger region of TG, limiting near-coastal thinning. This could result in delay or prevention of grounding-zone retreat from the stabilizing sill, but basin-wide thinning would still contribute to sea level rise and potentially trigger rapid basin-wide collapse if thinning progresses beyond a certain threshold.

* Corresponding author.
E-mail address: erc25@psu.edu (E.R. Clyne).

https://doi.org/10.1016/j.epsl.2020.116543
0012-821X/

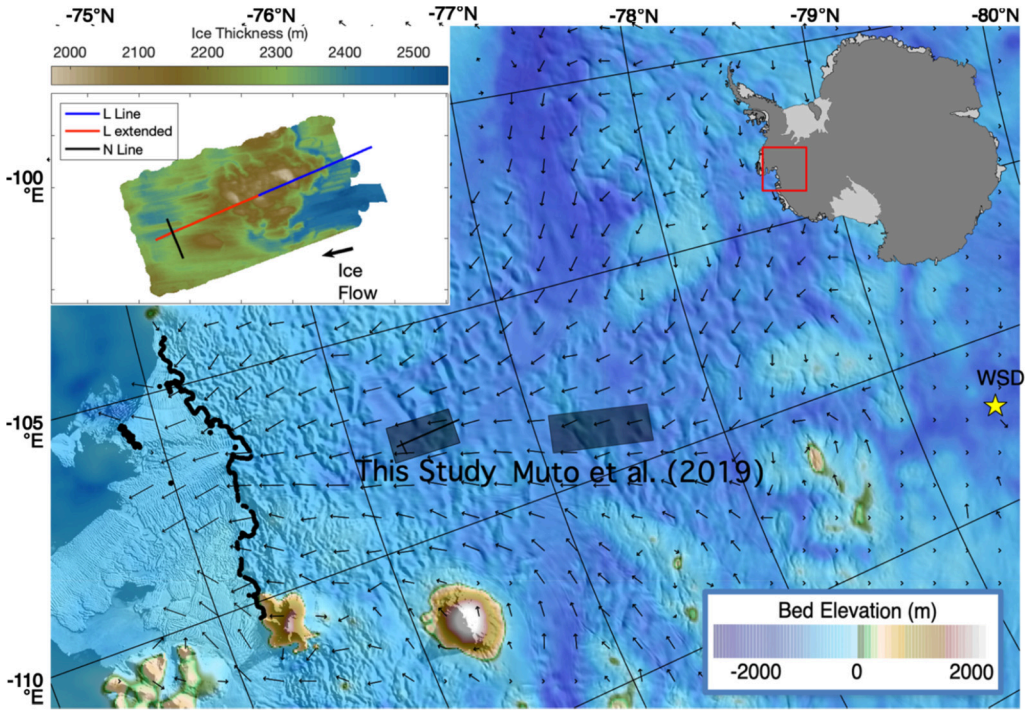

Fig. 1. Map showing L-Line (this study) in the context of TG and Antarctica. The line lengths on the main figure are indicative, and we refer readers to the inset for accurate lengths. Also shown is the study area of Muto et al. (2019a, 2019b), referenced in this paper. Co-located with the L-Line processed in this study is a radar-derived map of the bed (Holschuh et al., 2020), represented by the gray box overlapping the lines and the results shown in the upper left inset. Arrows show surface ice flow direction. Velocities in the study area are around 300 to 400 m yr^{-1} (Rignot et al., 2019; Mouginot et al., 2012).

A prior seismic survey focused on TG bed conditions showed highlands with either exposed bedrock, compacted tills, or very thin soft till on stoss-sides, and lee-sides and lowlands mantled in thick, soft till (Muto et al., 2019a, 2019b). Insights from laboratory and field studies (e.g., Weertman, 1957; Kamb, 2001; see summary in Koellner et al., 2019) indicate that the "hard" bedrock regions follow a nearly viscous sliding law, with soft till exhibiting more-nearly plastic behavior. Koellner et al. (2019) used a simplified flowline model to explore possible implications of this distribution of bed types, finding many situations in which modeled behavior over a mixed bed fell between the modeled behaviors for all-viscous and all-plastic end-members, but some situations in which mixed-bed behavior fell outside the end-members. Hence, it is important to know the actual distribution of bed types of TG extending closer to the grounding zone, and to incorporate this knowledge accurately in models.

As part of the effort to gain this information, 50 km of seismic data were collected approximately along flow, and an additional 9 km across flow, on TG 70 km downglacier of the observations of Muto et al. (2019a, 2019b). Along with the seismic data, swath radar data were collected and processed (Holschuh et al., 2020; inset, Fig. 1). Here we present the processed seismic data, and compare reflectivity and acoustic impedance with the swath radar-derived topographic map. This work serves as a baseline for further data collection and analysis. There is considerable variability in bed forms and properties, both within this dataset and upstream (Muto et al., 2019a, 2019b).

2. Data acquisition and processing

2.1. Reflection-seismic acquisition and processing

For logistical reasons, data for the 50 km line oriented along flow were collected in two 25-km segments using slightly different procedures, but yield broadly comparable results. The data along the upglacier 25 km (L-line, Fig. 1) were collected using a line of 48 receivers spaced 20 m apart and sources initiated every 480 m. Explosive charges ranging from 175 to 400 g were detonated at distances of +1920 m, +960 m, 0 m, and −960 m relative to the center of the spread (with positive values downglacier along the line). After the series of shots, half of the spread was moved forward (advancing 480 m) and the four-shot sequence was repeated, resulting in four-fold data. Each explosive hole was drilled to 90 m and used four times. For each use, a charge was lowered, the hole was backfilled with snow that was allowed to sinter for one day to improve coupling, and then the hole was shot. After detonation, the bottom of the hole was unusable and the subsequent shots were shallower. Shot depths thus ranged from 76 m to near the surface.

The receiver spread was composed of alternating conventional 28 Hz single-element geophones and georods (four 40 Hz geophone elements connected in series (Voigt et al., 2013)). All the geophones and georods were orientated to record vertically-traveling *P*-waves, and buried at 20 cm depth. Data were recorded at a sampling rate of 4000 Hz for 4 seconds to capture reflections from the ice bottom as well as the first multiple reflection. The peak frequency of the primary ice-bed reflection is ∼150 Hz, corresponding to a vertical resolution of ∼6.4 m and a pre-migration Fresnel zone of 315 to 350 m at the minimum and maximum thickness of ice.

To create the stacked images, individual shot gathers were inspected to remove noisy traces, after which a band-pass filter from 25 to 300 Hz, a top and bottom mute, an f-k (frequency-wavenumber) filter, and a predictive deconvolution filter were applied. A velocity of 3850 m s^{-1} was used for the normal moveout correction and for Kirchhoff time migration.

Static corrections were applied for the depth of each shot in the following way. The firn velocity-depth profile was determined from a shallow firn survey via the Wiechert-Herglotz method (e.g., Horgan et al., 2011; Shearer, 2019). This firn survey used a series

of hammer blows at the surface at 2 m increments into a spread of 48 geophones spaced 20 m apart, allowing the arrival times of the refracted waves through the firn to be picked in 2 m intervals. This firn model was used to estimate a static offset to a standard datum of 100 m below the surface. Traces were organized by common mid-point and stacked.

Additional survey data were collected extending the L-line 25 km downstream (L-Line-extended) using a spread of 96 receivers spaced 20 m apart. The spread was composed of the 48-receiver array described above with alternating georods and geophones, and a 48-receiver array of entirely 28 Hz geophones. The arrays were leap-frogged moving along the line. This geometry was also used to collect a 9.5 km cross line (N-Line; Fig. 1) across the L-Line-extended. The same filters and muting as described above were applied to L-Line-extended and N-Line. Shot depths along these lines varied from near-surface to 96 m depths. For these sources, regrettably, shot hole depths were not recorded due to errors on the part of the field team. For the analyses, we set all depths to 50 m, and we propagate the errors from the uncertain shot depths to the reflectivity uncertainties.

2.2. Seismic-amplitude analysis

To characterize the bed, we calculated the normal-incidence reflection coefficients and the bed acoustic impedance. For this study, any P-wave reflected from the bed at an incidence angle of less than 10° is considered as a normally incident ray. This limits the shots used to those with source-receiver offsets in the range of −480 m to 480 m. The methods used for the amplitude analysis are as outlined in Muto et al. (2019b). The reflection coefficients R_0 were calculated using the technique of Holland and Anandakrishnan (2009):

$$R_0 = \frac{A_1}{A_0}\frac{1}{\gamma_1}e^{\alpha d_1} \tag{1}$$

where A_1 is the amplitude of the primary ice-bed reflection, A_0 is the calculated source amplitude, α is the attenuation constant 2.7×10^{-4} m^{-1} (Horgan et al., 2011) $\pm 1.35 \times 10^{-4}$ m^{-1} (Muto et al., 2019b), γ_1 is the path amplitude factor (Medwin and Clay, 1998) for the path from source to receiver, and d_1 is the ray-path distance from source to receiver. The path amplitude factor for each receiver position was calculated by ray tracing through the firn and ice using the aforementioned velocity-depth profile, and d_1 was approximated as twice the ice thickness for all receivers in each shot, under the assumption of normal incidence rays. To calculate firn densities needed for the path amplitude factor, we used the inverted P-wave velocities and equation 2 of Kohnen and Bentley (1973).

To calculate the source amplitude A_0 of each shot, we used the multiple-path method for the N-Line; clear multiples were not always identifiable for the L-Line and L-Line-extended, so for them we used the direct-path method (Holland and Anandakrishnan, 2009). The multiple path method compares the primary ice-bed reflection amplitude A_1 to the first multiple amplitude A_2:

$$A_0 = \frac{A_1^2}{A_2}\frac{1}{2\gamma_1} \tag{2}$$

The direct-path method requires comparison of the direct-wave amplitudes at pairs of geophones chosen so that the source-receiver distance of the second geophone is twice that of the first geophone, thus simplifying the calculation to:

$$A_0 = \frac{B_1^2}{B_2}\frac{\gamma_2}{\gamma_1^2} \tag{3}$$

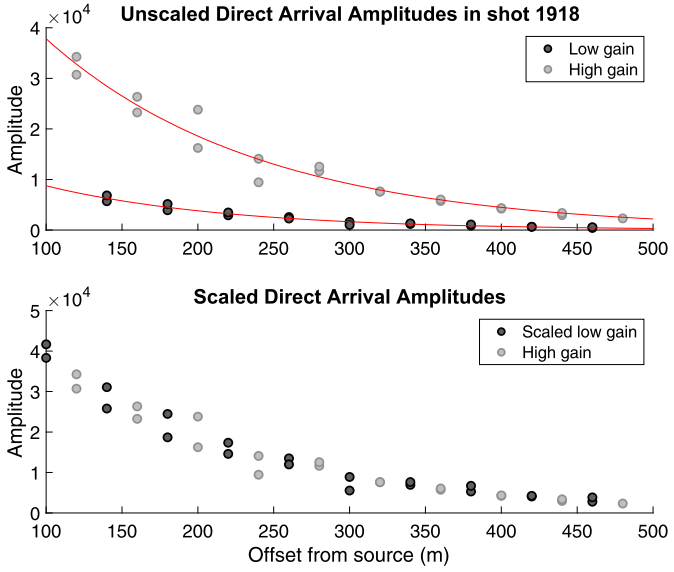

Fig. 2. Example of the gain scaling process. Top plots show the direct P-wave arrivals for the high-gain (light gray) and low-gain (dark gray) receivers plotted over distance from the source. The red lines are the exponential regressions. The bottom plots show the amplitude values after the low-gain values have been scaled to the high-gain values using the ratio of the exponential regression.

where B_1 and B_2 represent the direct P-wave arrival amplitudes of the geophone pair, and γ_1 and γ_2 their respective path-amplitude factors determined by ray tracing through the firn-velocity model. For both methods, the source amplitude and its uncertainty are taken as the mean A_0 and its standard deviation for each shot gather.

A_1, A_2, B_1 and B_2 were picked for each trace, treating the arrival wavelets as Ricker wavelets. The primary ice-bed reflections were often closely followed (if not overlapped) by secondary arrivals in regions with significant topography, complicating isolation of the wavelet. Thus, amplitudes were always picked using only the first lobe to avoid interference. The direct arrivals were clear Ricker wavelets with a negative backswing as the first lobe; thus, ice-bed reflections with negative-backswing first lobe were taken as 'normal' polarity reflections (higher acoustic impedance than ice), and reflections with positive-backswing first lobe were taken as 'reversed' polarity reflections (lower acoustic impedance than ice).

The geophones and georods have different sensitivities. The multiple-path method compares amplitudes between the primary and multiple at a receiver, so the sensitivity of the receiver is irrelevant. For the direct-path method we compare amplitudes at two different receivers, requiring a gain adjustment for arrival pairs that had a geophone and a georod. We determined a scaling factor k that is the ratio of the georod (high gain) and geophone (low gain) sensitivity. For each shot, the amplitudes of the direct P-wave arrivals vs. distance were fit by an exponential function. This was done separately for the georods and for the geophones using amplitudes picked from bandpass filtered data in the range where the frequency response of the two types of detectors is essentially flat. The ratio of the exponential fit equations was used to derive scaling factors, which were applied to the low-gain receivers (Fig. 2). This approach allowed a greater number of receiver pairs to be used in the calculation of A_0 than only comparing high-gain receivers, reducing the standard deviation of the calculated values. This scaling approach works for the direct arrival wave under the assumption that an exponential decay of amplitude with distance reasonably represents the change in amplitude with distance from the source. Some pairs were excluded because of noisy traces, or outlier amplitude values. The minimum number of pairs used for calculating A_0 was 4, and the average was 10.

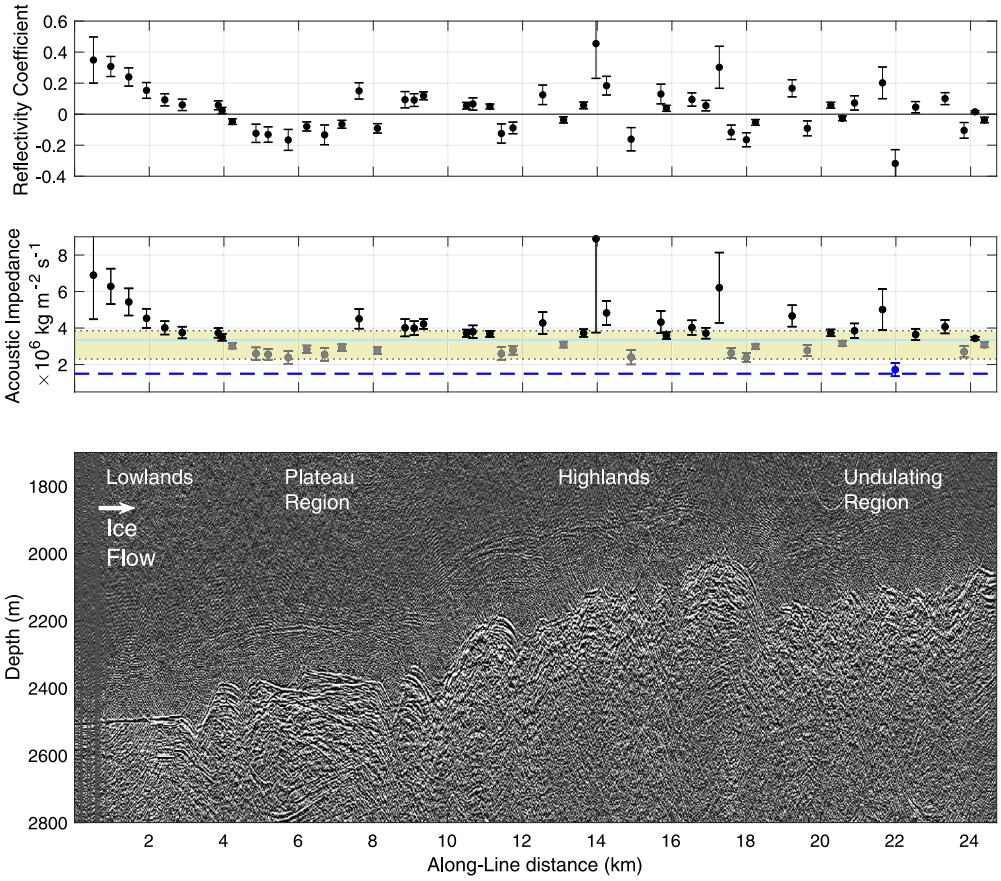

Fig. 3. L-Line, ice flow from left to right. Top: Reflection coefficient. Middle: Bed acoustic impedance. The R0 and Z0 mean values per shot gather are plotted with error bars. Also marked are the acoustic impedances of ice (light blue), water (dashed blue), and the range of till (yellow). The Z_b points are plotted as soft (gray), water (blue), or hard (black) relative to the ice acoustic impedance. The positions of the R_0 and Z_b along-line have been migrated to account for basal topography effects. Bottom: Migrated seismic line. Depth is with reference to the surface of the ice. (For interpretation of the colors in the figure(s), the reader is referred to the web version of this article.)

Gain-scaling was not attempted on the ice-bottom reflection when measuring A_1. The amplitude-analysis method depends on subtle changes in the amplitude of the ice-bottom reflection; thus, attempting to adjust the amplitudes via gain-scaling would compromise the result. A_0 represents the signal a receiver would measure if placed directly next to the source; hence, the low-gain receivers should use a different A_0 to calculate R_0 than the high-gain receivers. Since A_0 is calculated with respect to the high-gain receivers via the direct method in shots with alternating receiver types, only A_1 values measured on traces from high-gain receivers were used to calculate R_0 for these shots. The average number of usable traces in this case is 15, and the minimum used is 7. For any shots recorded using the same receiver types or with A_0 calculated using the multiple method, used all available A_1 and A_2 measurements were used to calculate R_0. The average number of usable traces in this case is 22, and the minimum used is 13.

Uncertainty in α and A_0 is as stated above. Uncertainty in bed depth for each shot was determined using an uncertainty in P-wave velocity of ± 70 m/s, determined from a velocity model of travel times in a region with no topography. Uncertainty in the path amplitude factor was determined as 1.9% by looking at the maximum possible error induced by varying shot depth from 2 m to 100 m, and adjusting ice thicknesses ± 100 m in the deepest and shallowest shot gathers. The uncertainty in A_1 was taken as the standard deviation of all usable values picked in each shot for the ice-bed reflection. The uncertainty in R_0 was taken as the larger of the standard deviation of all R_0 calculated per the shot or the weighted error propagated from A_0, A_1, d, γ and α via the law of propagation of uncertainty (e.g., Taylor and Kuyatt, 1994).

Once the reflection coefficients were determined, the acoustic impedance of the bed was calculated as (Sheriff and Geldart, 1995):

$$Z_b = Z_{\text{ice}} \frac{(1 + R_0)}{(1 - R_0)} \tag{4}$$

using a Z_{ice} of $3.33 \pm 0.04 \times 10^6$ kg m^{-2} s^{-1}. This value was originally derived for Kamb and Whillans ice streams by Atre and Bentley (1993), chosen under the assumption of a 5 m layer of basal ice at the pressure melting point. This Z_{ice} assumption has been used in prior seismic studies on Thwaites (Muto et al., 2019a, 2019b) and neighboring Pine Island Glacier (Smith et al., 2013; Brisbourne et al., 2017), among many other studies. The effect of using different Z_{ice} values and uncertainty is explored in the Results section. The uncertainty in Z_b was propagated from R_0 and Z_{ice}.

3. Results

3.1. Seismic profiles

We next provide a brief description of the seismic profiles along each line. We divide the lines into separate regions for ease of description (labeled in the profiles (Figs. 3, 4, 5) and radar map (Fig. 6)), highlight ice thickness in notable locations, and discuss topographic features and other interesting reflections. Recall that the L-Line and L-Line-extended are approximately parallel to surface ice flow, with the N-Line approximately perpendicular to surface ice flow. Also recall that the L-Line and L-Line-extended are one longer line, which we separate into two because of the switch

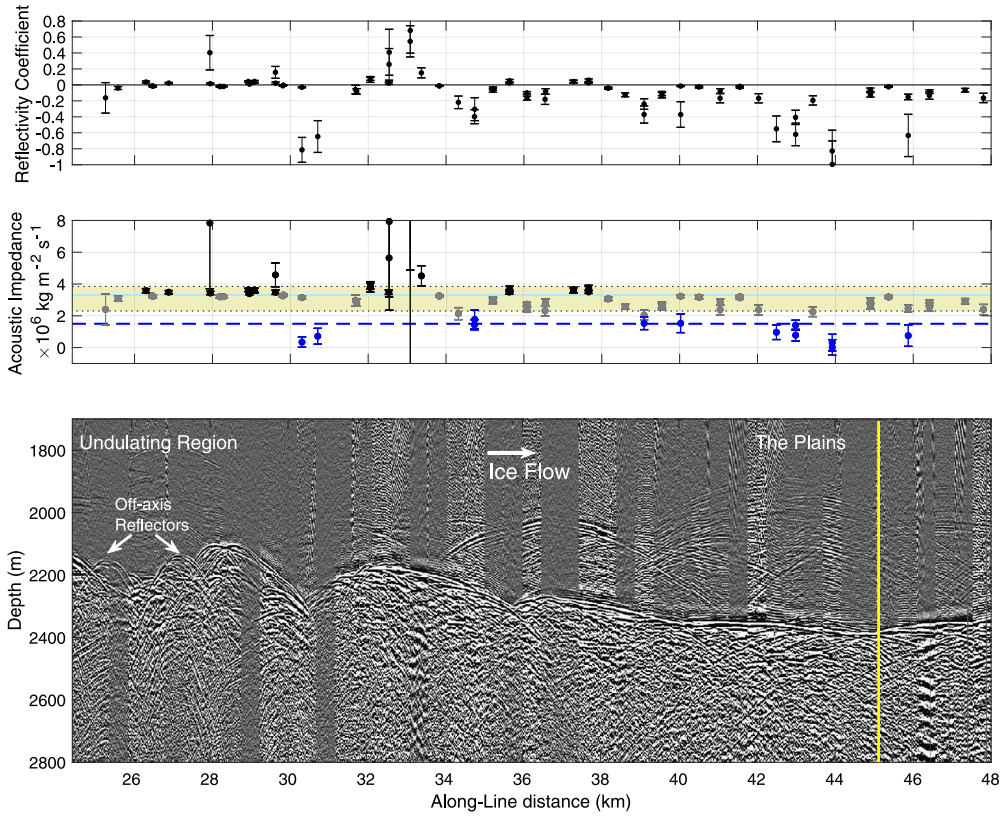

Fig. 4. L-Line-extended, ice flow from left to right. Top and Middle, same description as Fig. 3. Bottom: Unmigrated image. To produce the single fold image presented here, individual shots were aligned by hand. The yellow line indicates the cross point of N-Line. The profile is shown unmigrated, as the low fold and hand-adjusted shots created artifacts during migration.

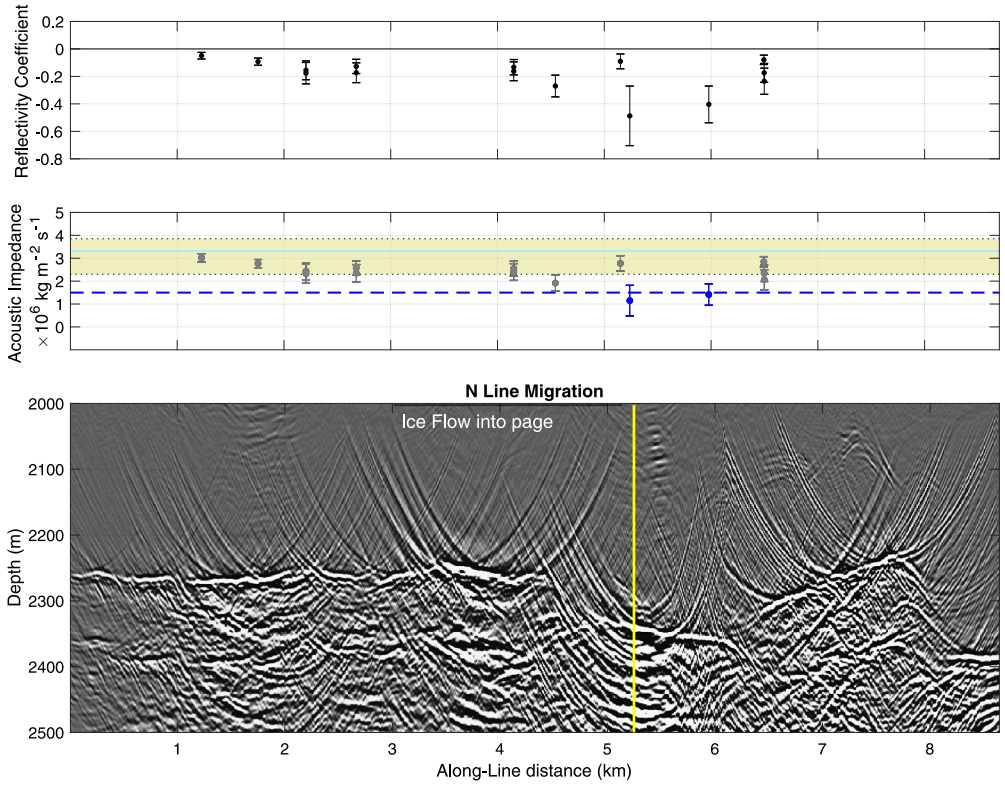

Fig. 5. N-Line. Top and Middle: same description as Fig. 3. Bottom: Migrated image of the crossflow N-Line, ice flow into the page. To produce the single fold images presented here, individual shots were aligned by hand. The yellow line indicates the crossing point with L-Line-extended. Notable features include the downstep in the bed around 4.5 km and a bump from 6.5 to 8 km along line with multiple internal reflectors.

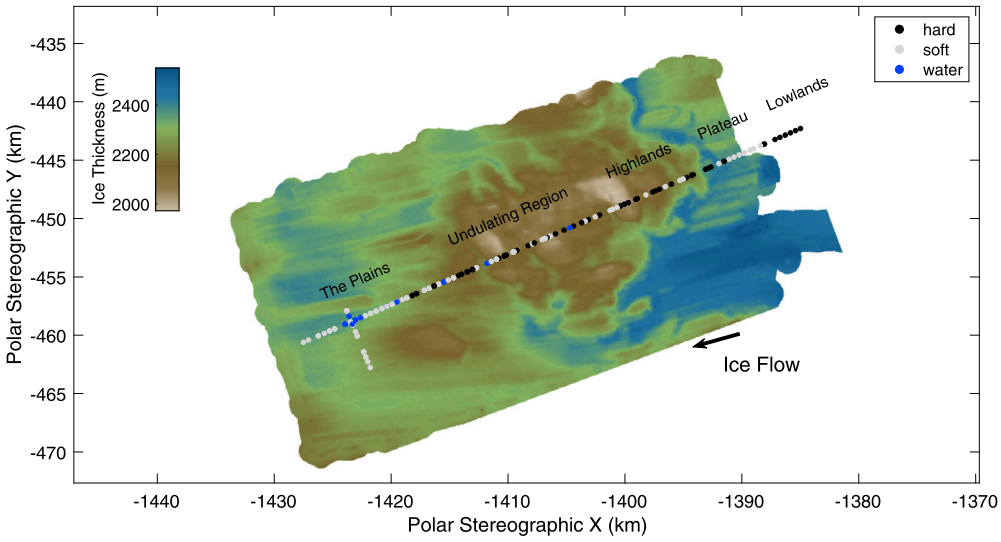

Fig. 6. Map of bed below Lower TG derived using radar. Color scale indicates ice thickness as depth below the ice surface. The acoustic impedances along the main line and crossline are plotted for reference: black is hard bed, gray is soft, and blue is water. Map provided by Nick Holschuh, analysis can be found in Holschuh et al. (2020).

in the way the seismic data were collected. It is worth noting that the main line is ∼10 to 15 degrees off the primary orientation of the bedforms in the radar map. The seismic line was not perfectly flow aligned, and the direction of flow curves slightly over the 50 km region surveyed, resulting in this slight offset.

3.1.1. L-Line

Starting at the upstream (left) end of the line (Fig. 3), the first 3 km are a flat lowland with an average ice thickness of ∼2500 m. The radar map does not extend quite as far upstream as the seismic line does, but extends similarly far upstream ∼10 km off-axis, and shows a similarly flat, deep, featureless bed there. Over the next 6 km downstream, the bed rises into a relatively flat plateau. Notable features atop the plateau, resolved by both radar and seismic data (Fig. 6), are possible crag-and-tail features, similar to those seen elsewhere by, e.g., Muto et al. (2019b) and King et al. (2007). These have relatively steep stoss-sides followed by elongated lee-side tails. Continuing downstream, there is a 10-km-long region of highlands with the greatest topographic relief observed along the line, including the highest point observed in the bed (Fig. 3 and 6; ∼2020 m ice thickness at 17.5 km along-line). The typical wavelength of the topography in the highlands along ice flow is 4 km, and the peak-to-trough amplitude ranges from 100 to 150 m. The highlands region slopes upwards ∼3% along ice flow. The downstream 5 km of L-Line is a region of gentle undulating topography, with ∼2 km wavelength and ∼50 m amplitude. This appears at the center of the region of high topography in the radar map (Fig. 6). In some regions (apparent in the unmigrated line), numerous reflectors are observed below the base of the ice that do not appear to be multiples or surface ghosts. These could be off-axis reflections, commonly observed elsewhere on TG (Muto et al., 2019b) and consistent with the widespread occurrence of nearby topography in the radar map. Additional data and analyses would be needed to learn whether any of these represent features within the subsurface. In the plateau region and highlands, englacial reflectors occur ∼100-200 m above the bed (cf. Horgan et al., 2011). They are less discernable over the lowlands and the undulating downstream end.

3.1.2. L-Line-extended

The undulating region in the L-Line continues another ∼10 km into L-Line-extended (Fig. 4). Two prominent reflectors that occur at 25.5 and 27 km likely arise from off-axis topography. Other off-axis reflectors may be present below the primary bed reflection, based on the occurrence of nearby bedforms in the radar data and general consistency between the other seismic reflectors and the radar map along the seismic line. At 29 km there is a steep-sloped depression (ice thickness ∼2300 m, green colored trough between bumps in Fig. 6) just before the last significant bump of the undulating region. The rest of the line, labeled “The Plains” in Fig. 4, is relatively smooth, gradually deepening and marked by a few depressions, and with no clear off-axis reflections. There may be some englacial reflectors above the undulating end of the line, but they are hard to discern, possibly due to low-fold data coverage rather than a lack of physical reflectors. The radar map (Fig. 6) depicts muted but well-defined topography in the Plains with flow-aligned elongated bedforms.

3.1.3. N-Line

The 8.5 km-long crossline (Fig. 5) is relatively flat with a step down in the bed from 2250 m depth to 2330 m around 4.5 km along-line, and a bump in the deeper region from 6.5 to 8 km. In the radar map the line appears to cross the lee-side tails of a large upstream bump at 0 km and a thin flow-aligned bedform at 6.5 to 8 km. The “ghost reflection” of the bed (from energy propagating upward from shots, reflecting off the surface, then down to the bed and back up) is visible along the entire line; this energy is referred to as a ghost because it follows all reflections and multiples by a fixed time. There are no clear off-axis reflections, likely due to less topographic variation than the main line (Fig. 6), consistent with a bed streamlined in the direction of ice flow. There are no clearly discernible englacial reflectors, possibly due to the low fold from processing issues rather than a lack of physical reflectors.

3.2. Amplitude analysis

We next provide a brief description of the calculated reflection coefficients and acoustic impedance of the ice-bed boundary, plotted above the seismic profiles (Fig. 3, 4, 5) and over the radar map (Fig. 6). For reference, the generally accepted values for the acoustic impedance of basal glacial ice ($Z_{\text{ice}} = 3.33 \pm 0.04 \times 10^6$ kg m^{-2} s^{-1}), fresh water ($Z_{\text{water}} = 1.5 \times 10^6$ kg m^{-2} s^{-1}), dilated till (2.3×10^6 kg m^{-2} s^{-1} to 3.8×10^6 kg m^{-2} s^{-1}) and lodged tills and bedrock ($> 3.8 \times 10^6$ kg m^{-2} s^{-1}) are plotted (e.g., Atre and Bentley, 1993; Muto et al., 2019a, 2019b; Brisbourne et al., 2017; Smith, 1997). In this study, we took any regions with $R_0 > 0$

and $Z_{bed} > 3.8 \times 10^6$ kg m^{-2} s^{-1} as indicative of compacted till or bedrock with porosities <0.3 and labeled them hard bed. Any regions with $R_0 < 0$ and $Z_{water} < Z_{bed} < Z_{ice}$ indicate porosities >0.3 to 0.45, consistent with dilated tills, and are labeled soft bed (Atre and Bentley, 1993; Muto et al., 2019a, 2019b; Riverman et al., 2019). Values between Z_{ice} and 3.8×10^6 kg m^{-2} s^{-1} fall in the upper limit of tills generally considered to be dilated. We define these as a 'hard' till due to having a higher acoustic impedance than ice. The behavior of till in this range is explored in Muto et al. (2019a) and summarized in section 4.1 of this paper. As discussed by Muto et al. (2019a), it is likely that soft tills are thick and highly dilated in lowlands and lee-side positions, and thinner (sub-seismic wavelength), somewhat more compacted and perhaps discontinuous in stoss-side positions, contributing to intermediate R_0 and Z_{bed}, which we label as hard. This has significant implications for changes in the ice-bed sliding/deformation mechanism (Muto et al., 2019a, 2019b; Koellner et al., 2019; Parizek et al., 2013).

We also considered the use of different Z_{ice} values. While there are no existing temperature measurements for this region, observations (Schroeder et al., 2014) and models (Joughin et al., 2009) suggest the base of the ice is everywhere at the pressure-melting point; thus, there is likely not much spatial variability in Z_{ice}. Ice thickness is over 2000 m in our study region, which places the bed well below the transition of bubbles to clathrates (Neff, 2014), indicating the basal ice is bubble-free. Bubble-free ice at the pressure-melting temperature has a density of ~917 kg m^{-3} (e.g. Byrd Station, Gow, 1970; GISP2, Gow et al., 1997). It is possible the basal ice may contain some debris; however, the relatively high geothermal heat fluxes (Schroeder et al., 2014; Shen et al., 2020) and heat of sliding favor basal melting and downward velocity of the basal ice, which thus is unlikely to have high debris concentration. Assuming up to 10% debris by weight and common crustal rock densities of 2500 kg m^{-3} yields a basal ice density range of 917 to 1050 kg m^{-3}. Using our P-wave velocity of 3850 ± 70 m s^{-1} and this density range of 983.5 ± 66.5 kg m^{-3} to estimate Z_{ice}, we arrive at 3.78×10^6 kg m^{-2} s^{-1} ±8.5%. Switching between the high-end and low-end values in this range has little effect on the overall patterns and results, except for shifting numerical values of bed character up or down slightly. So, following prior workers to make comparisons easy, we use Z_{ice} as determined in Atre and Bentley (1993).

3.2.1. L-Line

In the upstream lowlands (Fig. 3), we observe normal-polarity reflections and Z_b values higher than that of ice, which indicate the bed is hard, but with Z_b and inferred hardness decreasing along flow towards the first topographic feature rising out of the lowlands into the plateau. This feature, likely a crag-and-tail, appears to be hard on the stoss side and soft on the lee side, with acoustic impedances only slightly above and below that of ice, respectively, indicating a subtle change rather than a large transition. The tail appears to be soft sediment. The transition from the plateau region into the highlands is a depression with soft till on the lee side of the plateau and hard till on the stoss side of the first bump ramping up to the highlands.

Within the highlands the bumps of varying sizes all display the hard stoss/soft lee pattern previously observed (Fig. 3 and 6). Of particular note, at 14 km along line the acoustic impedance is high ($> 8 \times 10^{-6}$ kg m^{-2} s^{-1}) on the stoss side of topography, the highest value observed in L-Line. Even with broad error bars, the high acoustic impedance with R_0 of ~0.4 to 0.5 indicates that the bed is bedrock (e.g., Smith, 1997). Continuing downstream, the undulating region has smaller-scale topography than observed in the highlands and a greater degree of variability in bed type, including what may be a seismically thick water layer near km 22.

3.2.2. L-Line-extended

The upstream end of L-Line-extended (Fig. 4) is a continuation of the undulating region in the downstream portion of L-Line. Possible overlapping off-axis reflectors complicated the interpretation of ice-bottom properties (due to rough off-axis topography, Fig. 6). However, the general trend of hard-stoss and soft-lee is still evident in this region, with water-saturated till or water present in some lee regions. In particular, two regions with high acoustic impedances ($> 5 \times 10^{-6}$ kg m^{-2} s^{-1}) occur near the tops of bumps around 27 km and 33 km along-line. Downstream in the Plains, the ice-bed has high-amplitude reversed reflectors, and the acoustic impedances indicate alternating pockets of soft till and water.

3.2.3. N-Line

The N-Line (Figs. 5 and 6) crosses the main line in the downstream region of L-Line-extended, where the bed is predominantly soft till. The bed is consistently soft across the topography. This suggests that the hard stoss/soft lee pattern observed along flow arises from interactions caused by the flow. Additionally, the bedform from 6.5 to 8 km appears soft, and may be flanked by water or water-saturated till in the region between the bedform tails (Figs. 5 and 6).

4. Discussion

4.1. Hard stoss and soft lee

The finding of primarily hard beds on the stoss sides of bumps and soft beds in the lee of bumps or depressions coincides with observations elsewhere on TG (Muto et al., 2019a, 2019b) and Rutford Ice Stream (King et al., 2007). In the context of this study, some of the 'hard' regions ($> 3.85 \times 10^6$ kg m^{-2} s^{-1}) clearly are highly compacted till or exposed bedrock (those well above Z_{ice}). More commonly, 'hard' values were positive-polarity reflections with acoustic impedances in the range between ice and the upper end of dilated till, as defined in section 3.2 (i.e., 3.33×10^6 to 3.85×10^6 kg m^{-2} s^{-1}). Conceptually this case of 'hard' bed is described in Muto et al. (2019a) and summarized here. Changing subglacial hydraulic-potential when ice flow encounters a bed bump causes water to flow around a bump rather than over, coupling the ice more strongly with the till and thus increasing deformation in the till; continuity then causes the till layer to thin or become discontinuous. Such a case would produce seismic data indicating a bed harder than a seismically thick soft till layer but softer than a highly compacted till or bedrock substrate. A well-coupled, thin soft till layer will have different basal sliding dynamics than a thick soft till layer, closer to that of compacted till or bedrock, and thus is treated here as hard bed.

Topographic position (stoss/lee) appears to exert the largest control on the bed character, but there is no clear relation between the size of bed bumps and the length of the soft sediment in the lee. Consider, for example, the potential crag-and-tail feature (~40 to 60 m height assuming a till seismic velocity of 1800 m s^{-1}) in the plateau region, which has a long (1.5 km) tail of soft sediment, compared to the large highlands bumps (100 to 150 m height) with no notable elongated downstream tails. Instead, the lee-side tails appear to be especially elongated in regions of generally soft bed with low ice surface slope, whereas short tails are more common in the regions of more-widespread hard bed, greater topographic relief, and steeper ice surface slope.

Holschuh et al. (2020) identified 'stoss-side moats' that occur upstream of bed bumps and extend laterally around the sides of the bumps. There is a moat delineating the plateau region from the highlands region in the seismic data and the swath radar (8.5 km along line, Figs. 3 and 6). It is hypothesized (in Holschuh et al., 2020 and Alley et al., 2019) that these moats are formed by

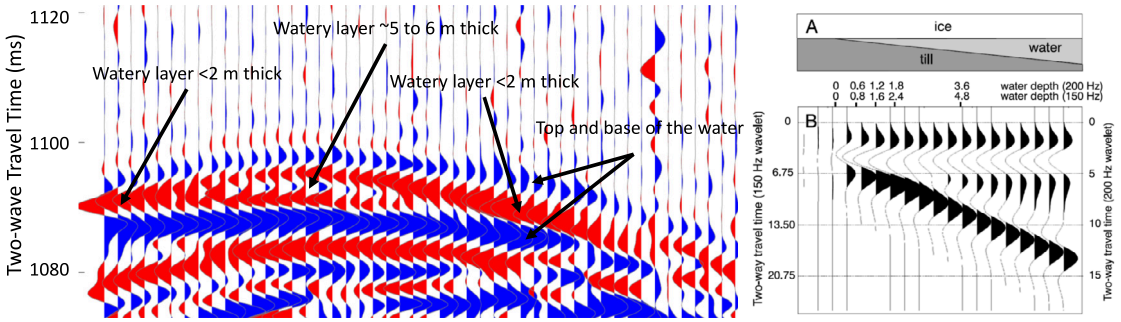

Fig. 7. Left: Shot gather with an acoustic impedance indicative of water/saturated till (1.7×10^6 kg m^{-2} s^{-1}) in the undulating region. Forwardswings are red and backswings are blue. Right: Annotated from Fig. 4 of King et al. (2004), showing A) their model of a layer of water between ice and compacted till and B) traces from 150 and 200 Hz seismic wavelets reflecting through the modeled layers.

the following steps: i) high pressure upglacier of bumps generated by ice flow against the topography diverts distributed water flow away from the bumps; ii) this causes ice to couple more strongly to any till present; iii) that till is then removed due to the stronger coupling, exposing bedrock to the ice and increasing erosion. This is consistent with our data showing a hard bed (around 4×10^6 kg m^{-2} s^{-1}) inside this moat. There are several additional cases of hard depressions occurring upstream of bed bumps in our data (3 km and 10 km in L-Line and 31 and 35.5 km in L-Line-extended), which may or may not have similar dynamics as larger distinct moats. It is also worth noting in Fig. 6 there is soft bed in the lee of the upstream lip of the moat. This may result from a low-pressure zone created by ice interaction with the lip, with possible implications for water routing and erosion (Muto et al., 2019b; Holschuh et al., 2020).

The highest acoustic impedances observed are in the lowlands and highlands of L-Line (Fig. 3), and two bumps in L-Line-extended (Fig. 4). The two bumps at 32.5 km and 33 km in L-Line-extended are particularly notable. The stoss values are $> 5 \times 10^6$ kg m^{-2} s^{-1}, with the highest values reaching well above 10×10^6 kg m^{-2} s^{-1}. These indicate exposed bedrock, especially at 33 km, which falls in the range of granite and metamorphic rocks (Eaton et al., 2003). Even with large error bars, the presence of a higher acoustic impedance material is supported by all shot gathers in this region indicating values in excess of till. Based on radar data, Schroeder et al. (2014) also argued that bedrock lacking significant sediment cover is observed along the lower trunk of Thwaites Glacier. Sedimentary rock units generally underly this region (e.g., Muto et al., 2016), but igneous intrusions may also occur (e.g., Behrendt et al., 1994; Wannamaker et al., 1996; Damiani et al., 2014).

N-Line crosses L-Line-extended in a region predominantly composed of soft till with locally seismically thick water layers (see below). The bump in N-Line from 6.5 to 8 km has steeply sloped flanks and multiple internal reflectors, which contrasts with the rest of N-Line. The bump appears to be a cross section of the elongated bedform that N-Line crosses in the radar data (Fig. 6), with acoustic impedance in the range of soft till. The bedform height is ~140 m, based on the difference in ice thicknesses over the bedform and the surrounding area as seen in the seismic profile and the radar map. In the radar map (Fig. 6) the low topography and elongated bedforms associated with these softer bed conditions appear to dominate the majority of the downstream region, suggesting much of it may have a similar character.

4.2. Water

There are several local regions along the main line with low acoustic impedances suggestive of water pockets. Most of these appear to occur in the downstream Plains region, associated with the soft bed there. However, in the undulating region of L-Line (Fig. 3 and 6), one of the soft lee sides exhibits a very low acoustic impedance just above that of water. In the shot gather there may be a reflection from the base of a saturated till/water layer with some interference from the ice-bed reflection (Fig. 7). It is possible that there is a water layer that is thinner than our seismic resolution of ~6.4 m. King et al. (2004) modeled the interference pattern of a 150-Hz wavelet (as is ours) as it passed through a layer of water between ice and compacted till. By comparing their findings to the wavelet structures observed in our data (Fig. 7), it appears there may be a pocket of water present over ~40 traces (400 m assuming a flat bed) with a maximum depth around 5 to 6 m and a minimum <2 m. All of the regions of especially low acoustic impedance along the main line appear similar. Additional work would be required, including additional modeling and probably additional data, to provide strong conclusions.

The deepest region of N-Line flanking the bedform has reflectivity and acoustic impedance values suggestive of water (5 to 6 km along-line, Fig. 5). Seismically thin layers may be involved, as along the crossing main line. The soft character of the bed in this region may account for the formation of numerous elongated bed features (Fig. 6).

5. Conclusions

Seismic and radar data from TG show stoss locations with exposed bedrock, hard till or thin/discontinuous soft till, alternating along-flow with thick soft till and possibly seismically thin water layers in lee-side positions. This is consistent with the findings of Muto et al. (2019a, 2019b) about 70 km farther upstream. Where the seismic line crosses a well-developed stoss-side moat, the bed is hard, supporting the hypothesis of Holschuh et al. (2020), although with a little soft material in the lee of the lip of the moat. These results provide a template for modeling ice-flow of TG, but highlight that most of the glacier's bed has not been surveyed in this way. To improve future predictions of TG's behavior, there is a high-priority need for high-resolution bed maps beneath the outlet glacier and its shear margins, to determine how basal rheology varies and to establish physically-based correlations between that variability and local basal topography and/or subglacial hydrology. This may be accomplished with a mixture of seismic surveying to directly measure acoustic impedance, and radar data for ice-thickness to determine where hard-stoss and soft-lee conditions should be applied.

CRediT authorship contribution statement

Elisabeth R. Clyne: Formal analysis, Software, Visualization, Writing - original draft, Writing - review & editing. **Sridhar Anandakrishnan:** Conceptualization, Data curation, Funding acquisition, Investigation, Methodology, Project administration, Resources, Supervision, Validation, Writing - review & editing. **Atsuhiro Muto:**

Methodology, Software, Supervision, Validation, Writing - review & editing. **Richard B. Alley:** Conceptualization, Funding acquisition, Supervision, Validation, Writing - review & editing. **Donald E. Voigt:** Data curation, Investigation, Supervision.

Declaration of competing interest

The authors declare that they have no known competing financial interests or personal relationships that could have appeared to influence the work reported in this paper.

Data availability

Lower Thwaites raw reflection seismic data are available at https://doi.org/10.26207/6tj1-a971.

Acknowledgements

This work was supported by the US National Science Foundation under grants NSF-1738934 and 1739003 (A.M., S.A., R.B.A., B.R.P., K.C., N.H.), NSF-0424589 (S.A., R.B.A.), NSF-1443190 (B.R.P., S.J.K.), by the National Aeronautics and Space Administration under grant NNX15AH84G (A.M., B.R.P., S.J.K.) and by The Heising-Simons Foundation, Grant Agreement #2018-0769 (S.A., R.B.A., B.R.P.).

We thank L. Stearns, L. Peters, L. Zoet, the PASSCAL Instrument Center, UNAVCO, Antarctic Support Contractor, and Kenn Borek Air for assistance with field data collection, Huw Horgan for providing help with the firn survey inversion, and Nicholas Holschuh for providing the processed swath radar map used in this publication.

This work is from the GHOST project, a component of the International Thwaites Glacier Collaboration (ITGC). Support from National Science Foundation (NSF PLR 1738934) and Natural Environment Research Council (NERC NE/S006672/1, NERC NE/S006621/1, NERC NE/S006613/1). ITGC Contribution No. ITGC-015.

References

Alley, R.B., Anandakrishnan, S., Christianson, K., Horgan, H.J., Muto, A., Parizek, B.R., Pollard, D., Walker, R.T., 2015. Oceanic forcing of ice-sheet retreat: West Antarctica and more. Annu. Rev. Earth Planet. Sci. 43, 207–231. https://doi.org/10.1146/annurev-earth-060614-105344.

Alley, R.B., Cuffey, K.M., Zoet, L.K., 2019. Glacial erosion: status and outlook. Ann. Glaciol. 60, 1–13. https://doi.org/10.1017/aog.2019.38.

Atre, S.R., Bentley, C.R., 1993. Laterally varying basal conditions beneath ice streams B and C, West Antarctica. J. Glaciol. 39, 507–514. https://doi.org/10.3189/S0022143000016403.

Bassis, J.N., Walker, C.C., 2012. Upper and lower limits on the stability of calving glaciers from the yield strength envelope of ice. Proc. R. Soc. A, Math. Phys. Eng. Sci. 468, 913–931. https://doi.org/10.1098/rspa.2011.0422.

Behrendt, J.C., Blankenship, D.D., Finn, C.A., Bell, R.E., Sweeney, R.E., Hodge, S.M., Brozena, J.M., 1994. CASERTZ aeromagnetic data reveal late Cenozoic flood basalts(?) in the West Antarctic rift system. Geology 22, 527–530. https://doi.org/10.1130/0091-7613(1994)022<0527:CADRLC>2.3.CO;2.

Brisbourne, A.M., Smith, A.M., Vaughan, D.G., King, E.C., Davies, D., Bingham, R.G., Smith, E.C., Nias, I.J., Rosier, S.H.R., 2017. Bed conditions of Pine Island Glacier, West Antarctica. J. Geophys. Res., Earth Surf. 122, 419–433. https://doi.org/10.1002/2016JF004033.

Christianson, K., Bushuk, M., Dutrieux, P., Parizek, B.R., Joughin, I.R., Alley, R.B., Shean, D.E., Abrahamsen, E.P., Anandakrishnan, S., Heywood, K.J., Kim, T.-W., Lee, S.H., Nicholls, K., Stanton, T., Truffer, M., Webber, B.G.M., Jenkins, A., Jacobs, S., Bindschadler, R., Holland, D.M., 2016. Sensitivity of Pine Island Glacier to observed ocean forcing: PIG response to ocean forcing. Geophys. Res. Lett. 43, 10,817–10,825. https://doi.org/10.1002/2016GL070500.

Damiani, T.M., Jordan, T.A., Ferraccioli, F., Young, D.A., Blankenship, D.D., 2014. Variable crustal thickness beneath Thwaites Glacier revealed from airborne gravimetry, possible implications for geothermal heat flux in West Antarctica. Earth Planet. Sci. Lett. 407, 109–122. https://doi.org/10.1016/j.epsl.2014.09.023.

Eaton, D.W., Milkereit, B., Salisbury, M.H., 2003. Hardrock Seismic Exploration. SEG Books.

Gow, A.J., 1970. Preliminary results of studies of ice cores from the 2164 m deep drill hole, Byrd Station, Antarctica. IASH 86, 78–90. http://hydrologie.org/redbooks/a086/086014.pdf.

Gow, A.J., Meese, D.A., Alley, R.B., Fitzpatrick, J.J., Anandakrishnan, S., Woods, G.A., Elder, B.C., 1997. Physical and structural properties of the Greenland Ice Sheet Project 2 ice core: a review. J. Geophys. Res., Oceans 102, 26559–26575. https://doi.org/10.1029/97JC00165.

Holland, C.W., Anandakrishnan, S., 2009. Subglacial seismic reflection strategies when source amplitude and medium attenuation are poorly known. J. Glaciol. 55, 931–937. https://doi.org/10.3189/002214309790152528.

Holland, P.R., Bracegirdle, T.J., Dutrieux, P., Jenkins, A., Steig, E.J., 2019. West Antarctic ice loss influenced by internal climate variability and anthropogenic climate forcing. Nat. Geosci. 12, 718–724. https://doi.org/10.1038/s41561-019-0420-9.

Holschuh, N., Christianson, K., Paden, J., Alley, R.B., Anandakrishnan, S., 2020. Linking postglacial landscapes to glacier dynamics using swath radar at Thwaites Glacier, Antarctica. Geology 48. https://doi.org/10.1130/G46772.1.

Horgan, H.J., Anandakrishnan, S., Alley, R.B., Burkett, P.G., Peters, L.E., 2011. Englacial seismic reflectivity: imaging crystal-orientation fabric in West Antarctica. J. Glaciol. 57, 639–650. https://doi.org/10.3189/002214311797409686.

Jenkins, A., Dutrieux, P., Jacobs, S., Steig, E.J., Gudmundsson, G.H., Smith, J., Heywood, K., 2016. Decadal ocean forcing and Antarctic ice sheet response: lessons from the Amundsen Sea. Oceanography 29, 106–117.

Joughin, I., Tulaczyk, S., Bamber, J.L., Blankenship, D., Holt, J.W., Scambos, T., Vaughan, D.G., 2009. Basal conditions for Pine Island and Thwaites Glaciers, West Antarctica, determined using satellite and airborne data. J. Glaciol. 55, 245–257. https://doi.org/10.3189/002214309788608705.

Joughin, I., Smith, B.E., Medley, B., 2014. Marine ice sheet collapse potentially under way for the Thwaites Glacier basin, West Antarctica. Science 344, 735–738. https://doi.org/10.1126/science.1249055.

Kamb, B., 2001. Basal zone of the West Antarctic ice streams and its role in lubrication of their rapid motion. In: The West Antarctic Ice Sheet: Behavior and Environment. American Geophysical Union (AGU), pp. 157–199.

King, E.C., Woodward, J., Smith, A.M., 2004. Seismic evidence for a water-filled canal in deforming till beneath Rutford ice stream, West Antarctica. Geophys. Res. Lett. 31. https://doi.org/10.1029/2004GL020379.

King, E.C., Woodward, J., Smith, A.M., 2007. Seismic and radar observations of subglacial bedforms beneath the onset zone of Rutford ice stream, Antarctica. J. Glaciol. 53 (183), 665–672. https://doi.org/10.3189/002214307784409216.

Koellner, S., Parizek, B.R., Alley, R.B., Muto, A., Holschuh, N., 2019. The impact of spatially-variable basal properties on outlet glacier flow. Earth Planet. Sci. Lett. 515, 200–208. https://doi.org/10.1016/j.epsl.2019.03.026.

Kohnen, H., Bentley, C.R., 1973. Seismic refraction and reflection measurements at "byrd" station, Antarctica. J. Glaciol. 12 (64), 101–111. https://doi.org/10.3189/S0022143000022747.

Medwin, H., Clay, C.S., 1998. Fundamentals of Acoustical Oceanography, Applications of Modern Acoustics. Academic Press, Boston.

Mouginot, J., Scheuchl, B., Rignot, E., 2012. mapping of ice motion in Antarctica using synthetic-aperture radar data. Remote Sens. 4, 2753–2767. https://doi.org/10.3390/rs4092753.

Muto, A., Alley, R.B., Parizek, B.R., Anandakrishnan, S., 2019a. Bed-type variability and till (dis)continuity beneath Thwaites Glacier, West Antarctica. Ann. Glaciol. 1 (9). https://doi.org/10.1017/aog.2019.32.

Muto, A., Anandakrishnan, S., Alley, R.B., Horgan, H.J., Parizek, B.R., Koellner, S., Christianson, K., Holschuh, N., 2019b. Relating bed character and subglacial morphology using seismic data from Thwaites Glacier, West Antarctica. Earth Planet. Sci. Lett. 507, 199–206. https://doi.org/10.1016/j.epsl.2018.12.008.

Muto, A., Peters, L.E., Anandakrishnan, S., Alley, R.B., Parizek, B.R., Christianson, K., Holschuh, N., 2016. Upper-Crustal Structures in Byrd Subglacial Basin, West Antarctica, Revealed by Ground-Based and Airborne Geophysical Data. AGU Fall Meeting Abstracts 22. 2016AGUFM. C22C..07M.

Neff, P.D., 2014. A review of the brittle ice zone in polar ice cores. Ann. Glaciol. 55, 72–82. https://doi.org/10.3189/2014AoG68A023.

Parizek, B.R., Christianson, K., Anandakrishnan, S., Alley, R.B., Walker, R.T., Edwards, R.A., Wolfe, D.S., Bertini, G.T., Rinehart, S.K., Bindschadler, R.A., Nowicki, S.M.J., 2013. Dynamic (in)stability of Thwaites Glacier, West Antarctica. J. Geophys. Res., Earth Surf. 118, 638–655. https://doi.org/10.1002/jgrf.20044.

Parizek, B.R., Christianson, K., Alley, R.B., Voytenko, D., Vankova, I., Dixon, T.H., Walker, R.T., Holland, D.M., 2019. Ice-cliff failure via retrogressive slumping. Geology 47 (5), 449–452. https://doi.org/10.1130/G45880.1.

Pollard, D., DeConto, R., Alley, R.B., 2015. Potential Antarctic ice sheet retreat driven by hydrofracturing and ice cliff failure. Earth Planet. Sci. Lett. 412, 112–121. https://doi.org/10.1016/j.epsl.2014.12.035.

Rignot, E., Jacobs, S.S., 2002. Rapid bottom melting widespread near Antarctic ice sheet grounding lines. Science 296, 2020–2023. https://doi.org/10.1126/science.1070942.

Rignot, E., Mouginot, J., Scheuchl, B., van den Broeke, M., van Wessem, M.J., Morlighem, M., 2019. Four decades of Antarctic ice sheet mass balance from 1979–2017. Proc. Natl. Acad. Sci. USA 116, 1095–1103. https://doi.org/10.1073/pnas.1812883116.

Riverman, K.L., Anandakrishnan, S., Alley, R.B., Holschuh, N.D., Dow, C.F., Muto, A., Parizek, B.R., Christianson, K., Peters, L.E., 2019. Wet subglacial bedforms of the NE Greenland ice stream shear margins and interior. J. Glaciol. 60 (80), 91–99. https://doi.org/10.1017/aog.2019.43.

Scambos, T.A., Bell, R.E., Alley, R.B., Anandakrishnan, S., Bromwich, D.H., Brunt, K., Christianson, K., Creyts, T., Das, S.B., DeConto, R., Dutrieux, P., Fricker, H.A., MacGregor, J., Medley, B., Nicolas, J.P., Pollard, D., Siegfried, M.R., Smith, A.M., Steig, E.J., Trusel, L.D., Vaughan, D.G., Yager, P.L., 2017. How much, how fast?: a science review and outlook for research on the instability of Antarctica's Thwaites Glacier in the 21st century. Glob. Planet. Change 153, 16–34. https://doi.org/10.1016/j.gloplacha.2017.04.008.

Schroeder, D.M., Blankenship, D.D., Young, D.A., Quartini, E., 2014. Evidence for elevated and spatially variable geothermal flux beneath the West Antarctic ice sheet. Proc. Natl. Acad. Sci. USA 111, 9070–9072. https://doi.org/10.1073/pnas.1405184111.

Shearer, P.M., 2019. Introduction to Seismology. Cambridge University Press.

Shen, W., Wiens, D., Lloyd, A., Nyblade, A., 2020. A geothermal heat flux map of Antarctica empirically constrained by seismic structure. Geophys. Res. Lett., e2020GL086955. https://doi.org/10.1029/2020GL086955.

Shepherd, A., Wingham, D., Rignot, E., 2004. Warm ocean is eroding West Antarctic Ice Sheet. Geophys. Res. Lett. 31. https://doi.org/10.1029/2004GL021106.

Sheriff, R.E., Geldart, L.P., 1995. Exploration Seismology. Cambridge University Press.

Smith, A.M., 1997. Basal conditions on Rutford ice stream, West Antarctica, from seismic observations. J. Geophys. Res. 102, 543–552. https://doi.org/10.1029/96JB02933.

Smith, A.M., Jordan, T.A., Ferraccioli, F., Bingham, R.G., 2013. Influence of subglacial conditions on ice stream dynamics: seismic and potential field data from Pine Island Glacier, West Antarctica. J. Geophys. Res., Solid Earth 118, 1471–1482. https://doi.org/10.1029/2012JB009582.

Taylor, B.N., Kuyatt, C.E., 1994. Guidelines for evaluating and expressing the uncertainty of NIST measurement results. In: NIST Technical Note 1297 1994 Edition. National Institute of Standards and Technology, Gaithersburg, MD, US.

Voigt, D.E., Peters, L.E., Anandakrishnan, S., 2013. 'Georods': the development of a four-element geophone for improved seismic imaging of glaciers and ice sheets. Ann. Glaciol. 54, 142–148. https://doi.org/10.3189/2013AoG64A432.

Wannamaker, P.E., Stodt, J.A., Olsen, S.L., 1996. Dormant state of rifting below the Byrd subglacial basin, West Antarctica, implied by magnetotelluric (MT) profiling. Geophys. Res. Lett. 23, 2983–2986. https://doi.org/10.1029/96GL02887.

Weertman, J., 1957. On the sliding of glaciers. J. Glaciol. 3, 33–38. https://doi.org/10.3189/S0022143000024709.